

### Stabilization of a Planetary-Explorer Balloon-Payload System using Tensegrity

#### Thomas Claudet

IMT Atlantique, Georgia Institute of Technology thomas.claudet1@gmail.com

#### Thomas Bewley

University of California San Diego, Aerospace Robotics and Control Lab bewley@ucsd.edu

#### Ryan Alimo

Jet Propulsion Laboratory, California Institute of Technology sralimo@jpl.nasa.gov

#### Abstract

This paper considers the stabilization of a Planetary-Explorer Balloon-Payload system designed around a tensegrity basis. Theoretical analysis and simulations show its robustness to wind loads by dynamically varying the tension of its tethers attaching it to the ground.

#### 1 Introduction

To go further and safer, NASA has developed cutting-edge robotic space exploration missions, such as with the Curiosity rover in 2011 on Mars, followed by Perseverance and Ingenuity, the new rover and first drone flying on another planet for JPL Mars 2020 mission. A part of their objectives is to explore interesting and intriguing areas of the planet. Between orbiters like Mars Reconnaissance and rovers, new autonomous vehicles are continued to be engineered to explore the hardest terrains: JPL's Limbed Excursion Mechanical Utility Robot [2], climbing from below using rock grippers, or Caltech's tethered two-wheeled Axel rover [3], descending via controlled rappel. Drones also allow the scientists to gather pictures and data of the terrain from a low-altitude point of view, thus helping to reveal the geological history of the planet, with stratified sedimentary rocks as observed in Valles Marineris, ancient lakeshore with Jezero Crater, transient environmental features at the poles like the areneiforms or particular objects of interest with the bright gully deposits in the western region of Hale Crater as shown in figure 1.

It is worth noting that on the one side, climbers are subject to delicate maneuvers and can potentially endanger the mission, and more importantly the environment. On the other side, drones like Ingenuity will have to spend a lot

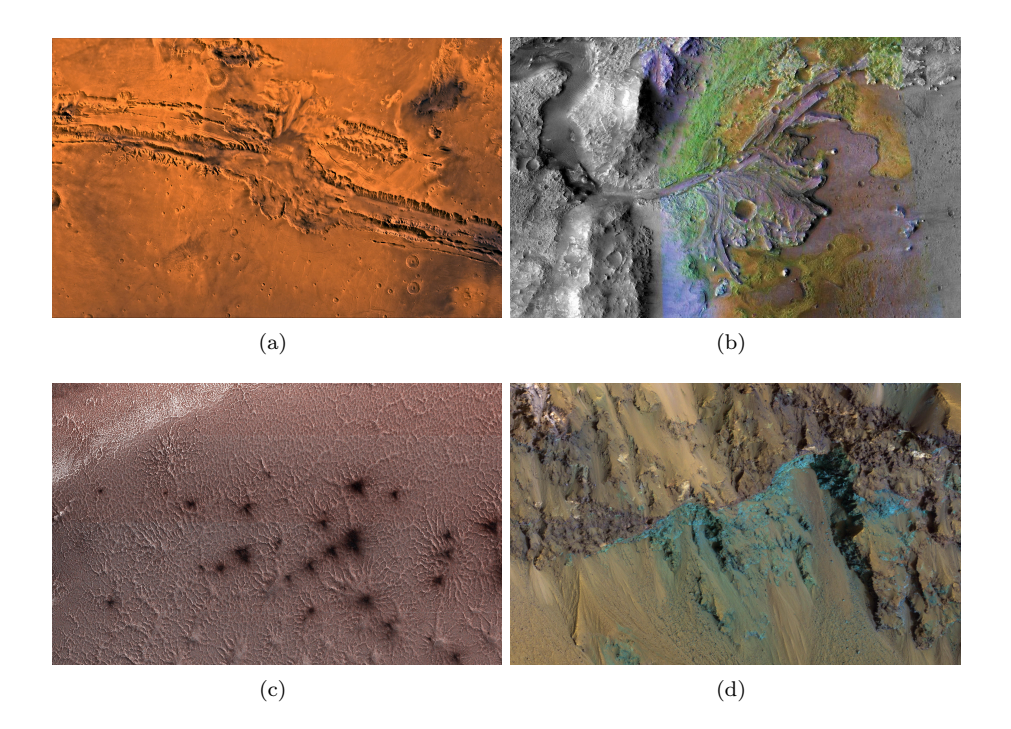


Figure 1: (a) Valles Marineris (b) Jezero Crater (c) Araneiforms at the poles (d) Gully deposits in Hale Crater [4]

of energy to lift the engine off the ground since Mars atmosphere density represents only 1% of the one on Earth, therefore allowing flights duration of only 90 seconds. In this paper, we present an in-between robotic structure able to get rid of all these constraints, and capable of conducting really precise experiments requiring extreme stabilization and handling very stormy conditions.

Over the past century, tensegrity, a structural equilibrium principle found in nature based on a network of tensile members such as bars and tethers has gained in popularity. First used for its beauty in art and architecture, it is now becoming a tool of primary choice in engineering and sciences for its mechanical advantages when one wants to design an optimal structure to minimize tensile, compression or bending loads [5, 6].

Here, the study first recalls the statics and dynamics governing the system [7]. It then focuses on the linearization of the system around its equilibrium state. The research subsequently sheds light on the open-loop analysis as well as closed-loop robustness by developing and comparing several controllers. It finally discusses and paves the way for neural networks usefulness in the system.

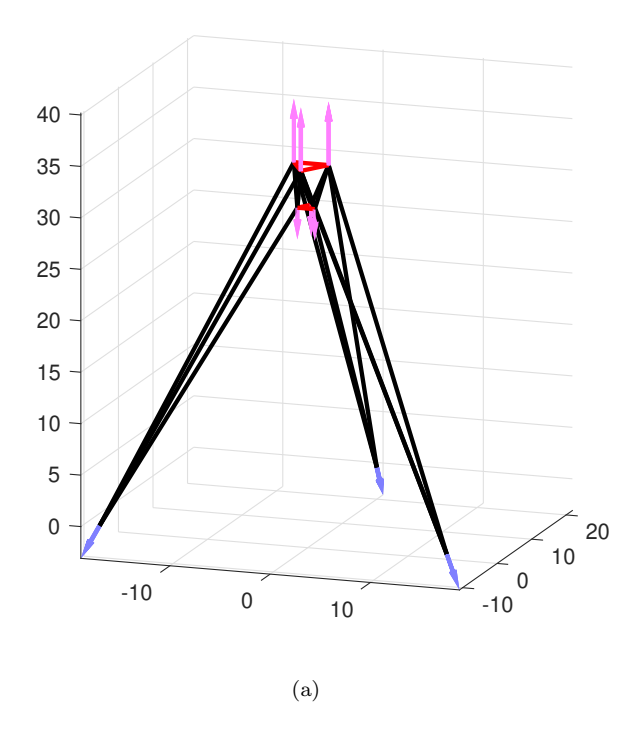


Figure 2: The Balloon-Payload system

#### 2 Problem formulation

#### 2.1 Static analysis of the tensegrity system

Following the mathematical background first written in [6] and applied is [7], this section will discuss the static analysis of this tensegrity structure shown in figure 2.

This tense grity system can be fully described by q free nodes:  $Q = [\vec{q_1},...,\vec{q_n}]$ , p fixes nodes:  $P = [\vec{p_1},...,\vec{p_n}]$  that form n = p + q nodes:  $N = [Q,P] = [\vec{n_1},...,\vec{n_n}]$ . They are linked to each other by s strings:  $S = [\vec{s_1},...,\vec{s_s}]$ .

Here, we have two subsystems: the balloon and the payload. They have their proper inertia matrix and we can choose the number of their attachment points. Threefold symmetry is explored in this paper, with q=6, p=3, n=9. Different structure configurations are also possible as seen in figure 3. For example, a different number of strings (as in S1 where s=12 when in S2, s=15), or other symmetries like fourfold exist as well.

We also define the length of each string  $l_k = ||\vec{s_k}||, k \in [1, ..., s]$ , normalized string vector  $\vec{d_k} = \vec{s_k}/l_k$ , stacked in  $D = [\vec{d_1}, ..., \vec{d_s}]$ .

Let us now connect the structure. From [6], we use what is called a connectivity

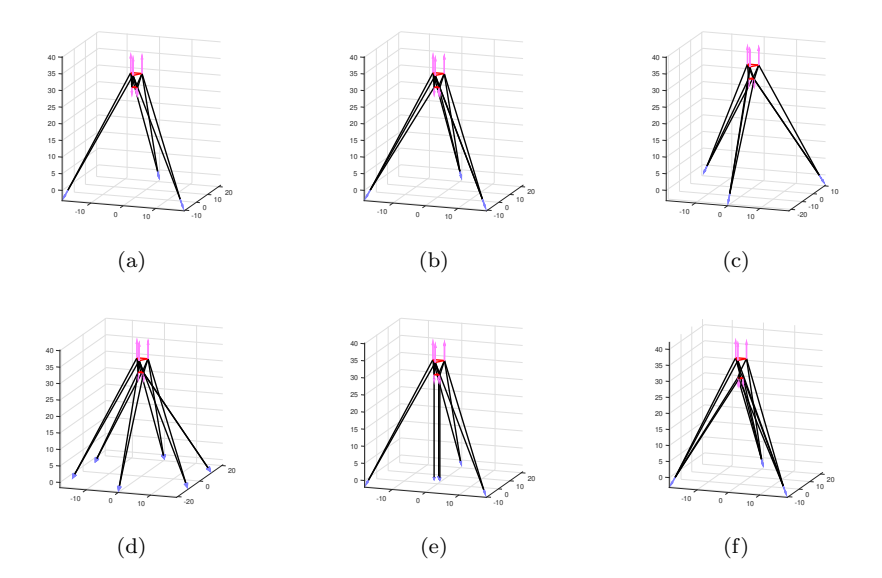


Figure 3: Design (a) S1 (b) S2 (c) S3 (d) S4 (e) S5 (f) S6

matrix C filled with 1,-1 or 0. In every line, there are zeros everywhere except in two columns: a -1 and a 1 representing the link between the two nodes at their given indices. In the threefold symmetry, we have 9 nodes, so C is a  $9 \times 9$  matrix. Note that we have  $S = NC^T$ .

We denote the external forces  $U=[\vec{v_1},...,\vec{v_q}]$  and the reaction forces  $V=[\vec{v_1},...,\vec{v_p}]$ , gathering them in W=[U,V]. The forces on each string  $\vec{s_k}$  at nodes  $n_{\vec{k},1}$  and  $n_{\vec{k},2}$  are  $\vec{d_k}x_k$  and  $-\vec{d_k}x_k$ . Thus, the internal string forces are DX with  $X=\operatorname{diag}(x_k)$ .

The total force in the system is then  $F = \left[\vec{f_1}, ..., \vec{f_n}\right] = -DXC$  with  $(f_i)_{i \in 1, ..., n}$  the total force at node i.

The equilibrium condition is then met when the internal forces are equal and opposite to the external forces: F = -W which can be also written as DXC = [U, V]. We finally solve for X.

String tensions are finally denoted, for all  $j \in [1, ..., s]$  by:

$$x_j^s = \max(0, \kappa_j(\|\vec{s_j}\| - l_j^{s,0})/l_j^{s,0}) \implies l_j^{s,0} = \frac{\kappa_j}{x_j^s + \kappa_j} \|\vec{s_j}\|,$$
 (1)

when  $\|\vec{s_j}\| > l_j^{s,0}$ , with  $l_j^{s,0}$  the rest length of string  $\vec{s_j}$  and  $\kappa_j$  its string constant. In cases where we have multiple solutions, minimum tensioning is found by solving an optimization problem. See [7] for more details.

#### Dynamic equations of motion

The equations governing the dynamics of the system are Newton-Euler's laws of rigid body motion applied to both the balloon and the payload, denoted  $(\sigma_k)_{k\in 1,2}$ , subjected to wind loads and originally written with the quaternion formalism in [7]:

$$\vec{r}_k^{\sigma} = \left(\sum_{i=1}^{a_k} \vec{f}_{k,i}^{\sigma} + \vec{u}_k^{\sigma}\right) / m_k^{\sigma},\tag{2}$$

$$\dot{\mathbf{d}}_{k}^{\sigma} = \mathbf{d}_{k}^{\sigma} \vec{\omega}^{\sigma,B} / 2, \ \dot{\vec{\omega}}^{\sigma,B} = \begin{pmatrix} [\tau_{k,1}^{\sigma,B} - (J_{k,3}^{\sigma} - J_{k,2}^{\sigma})\omega_{k,2}^{\sigma,B}\omega_{k,3}^{\sigma,B}] / J_{k,1}^{\sigma} \\ [\tau_{k,2}^{\sigma,B} - (J_{k,1}^{\sigma} - J_{k,3}^{\sigma})\omega_{k,3}^{\sigma,B}\omega_{k,1}^{\sigma,B}] / J_{k,2}^{\sigma} \\ [\tau_{k,3}^{\sigma,B} - (J_{k,2}^{\sigma} - J_{k,1}^{\sigma})\omega_{k,1}^{\sigma,B}\omega_{k,2}^{\sigma,B}] / J_{k,3}^{\sigma} \end{pmatrix},$$
(3)

where

$$\vec{\tau}_k^{\sigma,B} = \sum_{i=1}^{a_k} \vec{n}_{k,i}^{\sigma,B} \times [(\mathbf{d}_k^{\sigma})^* \vec{f}_{k,i}^{\sigma} \mathbf{d}_k^{\sigma}] + \vec{\eta}_k^{\sigma,B} \times [(\mathbf{d}_k^{\sigma})^* \vec{u}_k^{\sigma} \mathbf{d}_k^{\sigma}], \tag{4}$$

with:

 $(a_k)_{k\in 1,2}$ : number of nodes of solid body  $\sigma_k$ ,

 $\vec{r}_k^{\sigma}$ : position of solid body  $\sigma_k$  in the global reference frame,

 $\vec{f}_{k,i}^{\sigma}$ : internal force acting on  $\sigma_k$  at node  $i \in [1, a_k]$ ,

 $\vec{u}_k^{\sigma}$ : external force on  $\sigma_k$ ,

 $m_k^{\sigma}$ : mass of  $\sigma_k$ ,

 $\mathbf{d}_{k}^{\sigma}, \dot{\mathbf{d}}_{k}^{\sigma}$ : quaternion for angular deflection of  $\sigma_{k}$  and its derivative,

 $\vec{\omega}_k^{\sigma,B}, \vec{\omega}_k^{\sigma,B}$ : rate of rotation and acceleration of  $\sigma_k$  in body coordinates B,  $\vec{\sigma}_k^{\sigma,B}, \vec{\omega}_k^{\sigma,B}$  is [1, 2], ith contrast of  $\vec{\sigma}_k$  in body coordinates B,

 $\vec{\tau}_{k,i}^{\ddot{\sigma},B}, i \in [1,3]: i^{th}$  component of the external torque on  $\sigma_k$  in B,

 $J_{k,i}^{\sigma}, i \in [1,3]: i^{th}$  component of the inertia matrix of  $\sigma_k$ ,

 $\vec{n}_{k,i}^{\sigma,B}, i \in [1, a_k]$ : position of the  $i^{th}$  attachment point of  $\sigma_k$  in B,

 $\bar{\eta}_{l}^{\sigma,B}$ : moment arm of  $\sigma_k$  in B.

#### 2.3Conversion from quaternions to Euler Angles with Tait-Bryan rotation sequences

To get rid of the norm constraint  $\|\mathbf{d}_{k}^{\sigma}\| = 1$  during the linearization, we choose to convert quaternions to Euler angles  $(\theta, \phi, \psi)$  and to use Tait-Bryan (yawpitch-roll) rotation sequences which are defined by the following matrices:

$$R_{\theta} = \begin{bmatrix} 1 & 0 & 0 \\ 0 & \cos \theta & -\sin \theta \\ 0 & \sin \theta & \cos \theta \end{bmatrix}, \quad R_{\phi} = \begin{bmatrix} \cos \psi & 0 & \sin \phi \\ 0 & 1 & 0 \\ -\sin \phi & 0 & \cos \phi \end{bmatrix}, \quad R_{\psi} = \begin{bmatrix} \cos \psi & -\sin \psi & 0 \\ \sin \psi & \cos \psi & 0 \\ 0 & 0 & 1 \end{bmatrix},$$

with the complete rotation and anti-rotation matrices:

$$R_{\psi,\phi,\theta} = R_{\psi}R_{\phi}R_{\theta}, \quad R_{\theta,\phi,\psi} = R_{\psi,\phi,\theta}^{-1}.$$
 (5)

The system never reaches any singularities since the angles in the non-linear simulations using quaternions were very far away from  $\pi/2$  radians even with a strong wind.

#### 2.4 Linearization and state-space representation

In order to control this non-linear multi-input multi-output highly-coupled system effectively, we will put it in state-space form by linearizing it in the vicinity of the equilibrium previously found by the static analysis.

Both the balloon and the payload have 6 degrees of freedom: 3 for translations denoted 'r' and 3 for rotations 'd' along and around the (x,y,z) axis. It follows that the state vector will be composed of these variables and their first derivatives, leading to a  $2 \times ((3+3) \times 2) = 24$ -component state vector.

$$\vec{x} = [r_x^p, r_y^p, r_z^p, r_x^b, r_v^b, r_z^b, \dot{r}_x^p, \dot{r}_y^p, \dot{r}_z^p, \dot{r}_z^b, \dot{r}_v^b, \dot{r}_z^b, d_x^p, d_y^p, d_z^p, d_x^b, d_u^b, d_z^b, \dot{d}_y^p, \dot{d}_z^p, \dot{d}_y^b, \dot{d}_y^b, \dot{d}_z^b, \dot{$$

We actuate the structure by dynamically varying the rest length of the strings from the ground to the subsystems. In practice, this could be made by a set of rovers of other autonomous robots on the surface of the explored planet.

The command vector is then:

$$\vec{u} = [l_1^0, ..., l_m^0],$$

with m depending on the configuration and the symmetry (see figure 3). In the following, we drop the vector superscript for simplicity.

We then compute the Jacobian of the system around its equilibrium position to get the linearized state-space form:

$$\tilde{x} = A\tilde{x} + B\tilde{u} + Ew,\tag{6}$$

$$y = C\tilde{x} + D\tilde{u},\tag{7}$$

with:

$$A = \frac{\partial F}{\partial X}\bigg|_{x_{eq}, u_{eq}}, \ B = \frac{\partial F}{\partial U}\bigg|_{x_{eq}, u_{eq}} \ C = \frac{\partial G}{\partial X}\bigg|_{x_{eq}, u_{eq}}, D = \frac{\partial G}{\partial U}\bigg|_{x_{eq}, u_{eq}}, \quad \ (8)$$

$$\dot{x} = F(x, u, t), \ y = G(x, u, t),$$
 (9)

$$\tilde{x} = x - x_{eq}, \ \tilde{u} = u - u_{eq}, \tag{10}$$

with  $\vec{w} = [w_x^p, w_y^p, w_z^p, w_x^b, w_y^b, w_z^b]^T$  the disturbance (wind) vector and E the disturbance matrix composed of zeros and 1/m terms found in Newton's law. Finally, the system does not have a direct feedthrough, so D = 0.

#### 3 Open-loop analysis

Design S2 from figure 2 will be used.

#### 3.1 Natural behavior of the system

This section will discuss the open-loop analysis of the system, so when it is not controlled yet and oscillates under the wind loads.

Figure 4 represents the evolution of the horizontal and angular deflection states in function of time when the balloon is subject to a 50 N wind load along the Y-axis:  $w_u^b = 50N$ .

Since the system is symmetric with respect to the (YZ) plane, having wind loads in the Y-direction only moves and rotates the system in this plane. This also explains why only the angle around the X-axis, orthogonal to the plane, evolves over time.

Regarding the damping force, we have two main models: linear with  $\vec{F} = -b\vec{v}$  at low Reynolds ( $R_e < 0.1$ ), and quadratic:  $\vec{F} = -\frac{1}{2}\rho C_d S v^2 \frac{\vec{v}}{\|v\|}$  at relatively high velocity ( $R_e > 1000$ ), defining  $R_e$  as:

$$R_e = \frac{vL}{\nu}, \ \nu = \frac{\mu}{\rho},\tag{11}$$

with:

v the flow speed, L the characteristic linear dimension,  $\nu$  the kinematic viscosity of the fluid,  $\rho$  the density of the fluid,  $\mu$  the dynamic viscosity of the fluid.

We will stay in the linear case with respect to the testing parameters with a damping coefficient of -1.

Under the wind, the uncontrolled system could oscillate a lot and for a long time before eventually going back to a new equilibrium, which would certainly not be the first one if the wind stays a non-zero constant vector (see figure 4).

#### 3.2 Eigen and singular values

In order to better understand the system, it is always useful to compute the eigenvalues as well as the singular values of the state matrix.

For the eigenvalues, we will first solve for the roots  $\lambda$  of the characteristic polynomial  $\det(A - \lambda I_d)$ . The singular values are obtained by transforming the A matrix into the  $U\Sigma V^*$  form and by taking the diagonal elements of  $\Sigma$ . A plot of these values is displayed in figure 5.

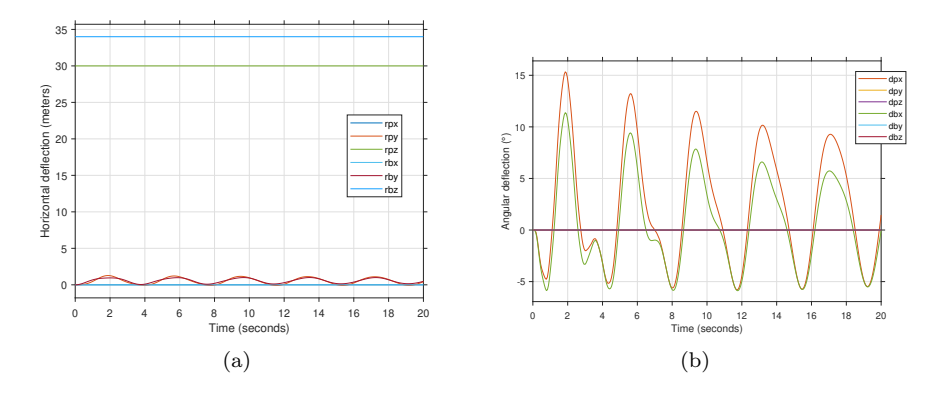


Figure 4:  $w_y^b = 50N$  (a) Horizontal deflection (b) Angular deflection

The 24 eigenvalues are all set in the left-half plane, which implies that the system is stable as extrapolated from figure 4. However, four of them are really close to 0, which means that the system is on the verge of instability. Some eigenvalues are very oscillatory with a relatively large imaginary part of 50. The system is slow because all the real parts are less than -0.5. We confirm this analysis with figure 4.

From them, we compute the natural frequencies and damping ratios which are indeed the ones found in the singular values plot and, as we will discuss later, in the Bode plot. The two high double peaks (if seen from very close) correspond to the eigenvalues close to 0, when the others all have a gain at their natural frequency less than 50dB. We tested the system with a constant wind, which would make inputs frequencies low and therefore attenuate the outputs. However, in cases when the wind would have a frequency closer to the different peaks, the system, if not actuated, would be subjected to strong resonances that may break it.

#### 3.3 Bode Plots

Because this is a multi-input multi-output system, Bode plots cannot be found for the entire system, but only between one input and one output of it. Because the test was with wind in the Y-direction which made the system oscillate in the (YZ) plane, we show the Bode plot of the transfer function between one of the tethers and  $r_y^p$  as well as  $d_x^p$  in figure 5. Note that using the other inputs would change some peaks position but the analysis would remain essentially the same.

We see resonances for the horizontal deflection and both resonances and antiresonances for the angular deflection. They are positioned at the same frequencies as the singular values plot, which then confirm it. The system acts as a natural low-pass filter, even if low frequencies are already slightly attenuated. This means that for input frequencies approximately above 50Hz, the inertia of the system would be too high to instantly make it respond to these inputs.

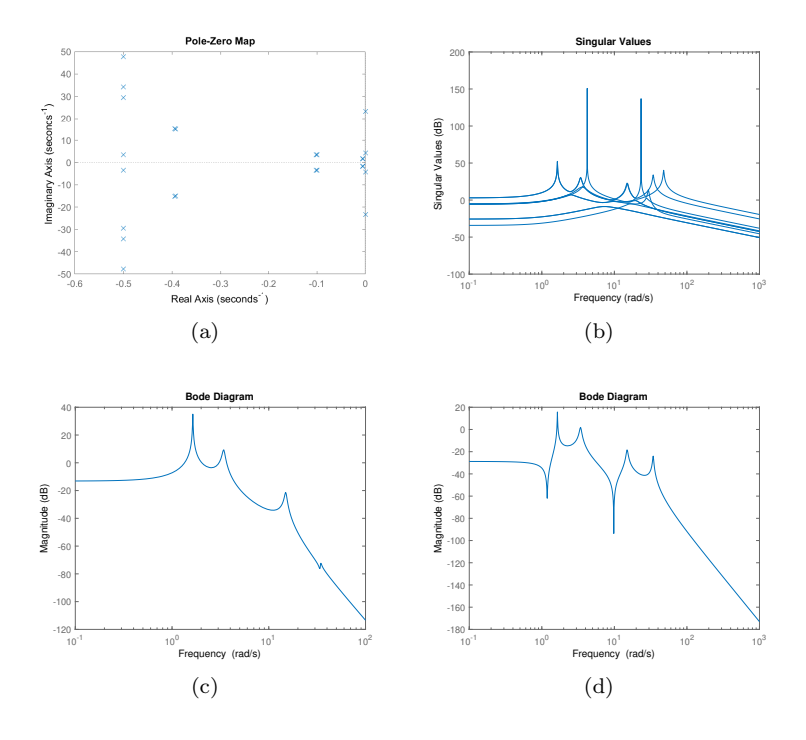


Figure 5: (a) Eigen values, (b) Singular values, (c) Bode Diagram of  $u_1 \to r_x^p$ , (d) Bode Diagram of  $u_1 \to d_x^p$ 

#### 3.4 Controllability and Observability

We now want to check whether the system is controllable and observable or not.

The ranks of the controllability and observability matrices are full:

$$\mathscr{C} = \begin{bmatrix} B & AB & \cdots & A^{n-1}B \end{bmatrix}, \qquad \mathscr{O} = \begin{bmatrix} C & CA & \cdots & CA^{n-1} \end{bmatrix}. \tag{12}$$

This result is enforced by the gramian criterion which states that for all t > 0, all the eigenvalues of the transitionary controllability and observability gramians are positive:

$$\int_{0}^{t} e^{At} B B^{T} e^{A^{T} t} dt > 0, \qquad \int_{0}^{t} e^{A^{T} t} C^{T} C e^{At} dt > 0.$$
 (13)

We can therefore conclude that the system is indeed controllable and observable.

### 4 Model-based controller design

From the previous section, the system has all the desirable properties needed to be well-actuated. We will now build model-based controllers that will dynamically output the strings rest lengths to be achieved in order to counter the wind effects on the structure.

# 4.1 First approach with the Linear-Quadratic Regulator (LQR)

The first controller that we develop in this paper is the Linear-Quadratic Regulator (LQR). It needs to know all the states but has really robust properties such as infinite gain margin, 60° phase margin a modulus margin greater than 1.

We will find a multivariable gain  $K_c$  such that  $u(t) = -K_c x(t)$ , and which minimizes the following cost function:

$$J = \int_0^\infty x^T Q x + u^T R u \, dt, \tag{14}$$

with

$$Q = Q^T \ge 0, \ R = R^T > 0. \tag{15}$$

In this paper, we also propose three different sets of weight matrices Q and R that we will compare. We will first be playing with R as a parameter  $\rho$  while letting Q as the identity matrix. We will then use diagonal matrices with values relative to the importance of the state. We will finally introduce the not sufficiently known but extremely useful De Larminat weight matrices, first introduced in [8] where the transitionary gramians have to be computed, and appearing in the expressions of Q and R, will allow us to place all the poles of the closed-loop system in the left of the vertical line  $-\frac{1}{T_c}$ , with  $T_c$  the control horizon time, a single tuning parameter to achieve the desired time response of the system.

After writing the Hamiltonian matrix and solving for P in the algebraic Riccati's equation:

$$A^T P + PA - PBR^{-1}B^T P + Q, (16)$$

we finally obtain:

$$K_c = -R^{-1}B^T P. (17)$$

It is now time to close the loop with this gain and analyse the results. With the first weight matrices set, we obtain the plots (a,b) in figure 6 for  $\rho = 0.1$ , (c,d) for  $\rho = 10$ .

All the poles are on the left-half plane, meaning that the system is stable. We see that decreasing  $\rho$  reduces the energy of the controller since the poles are slower. The time response become pseudo-periodic and the static error grows. Conversely, increasing  $\rho$  makes the system aperiodic and faster. However, it pumps more energy to the command and reduces the static error. At the extreme, we state that  $\lim_{\rho\to\infty} K_c$  is the Minimum-Energy-Stabilizing Controller whereas  $\lim_{\rho\to 0} K_c$  makes the system infinitely fast with an infinite amount of energy that the system cannot handle and it achieves zero steady-state error.

Then, in (e,f), we use diagonal weight matrices, with states that matter getting a weight of 1000, the others receiving 0.

This solution works well and use less energy than the one with small  $\rho$ .

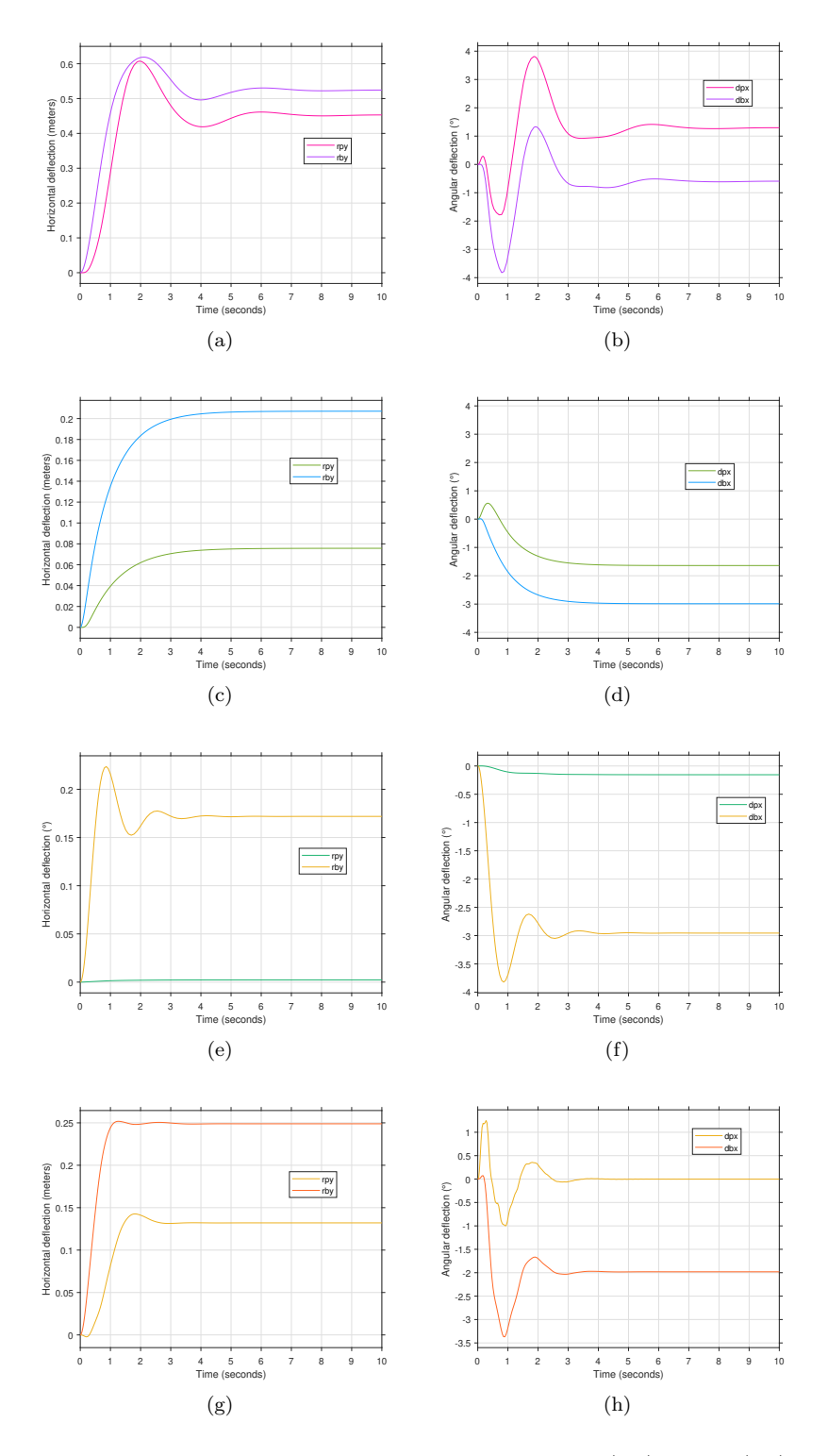


Figure 6: LQR Control: Horizontal and angular deflections: (a,b)  $\rho=10$  (c,d)  $\rho=0.1$  (e,f) Diagonal weight matrices (g,h) De Larminat weight matrices

In (g,h), De Larminat weight matrices are found with the following formulae (see [8] for more details):

$$Q = \left(T_c \int_0^{T_c} e^{At} B B^T e^{A^T t} dt\right)^{-1}, \quad R = Id$$
 (18)

Setting the approximate time response of the system is done by tuning this parameter  $T_c$  directly to the desired value. We found that for a unique  $T_c$  and for every wind vector, the system was able to achieve perfect tracking, but only for one state, the one that would then matter the most. This solution is certainly not acceptable and we will have to find better controllers in the following parts.

### 4.2 Steady-state error cancellation on important states with the Linear-Quadratic-Integral Regulator (LQI)

In this model-based controller design section, we finally approach the Linear-Quadratic-Integral Regulator to achieve zero steady-state errors on states that matter the most (ie: the payload ones). Here, we are still obliged to know all the states to perform these calculations. To do so, we work with the augmented system  $X = \begin{bmatrix} X^T & X_e^T \end{bmatrix}^T$  with X all the states of the system, and  $X_e$  the integrated states of the payload that matter (horizontal displacement and angular deflection). We then solve the LQR problem with this augmented system and find a gain  $K = \begin{bmatrix} K_p & K_i \end{bmatrix}$  such that

$$u = \begin{bmatrix} K_p & K_i \end{bmatrix} \begin{bmatrix} X \\ X_e \end{bmatrix} \tag{19}$$

In the curves shown in figure 7, we effectively confirm that the payload states are converging to zero when the other states are also very close to it, meaning that for these particular states, we came back to their equilibrium point found in the static analysis. Because we have used De Larminat weight matrices to get the controller gain, we can easily set the desired time response, with a lower bound given by the ability of the actuators to follow the required dynamics (see figure 7 (c)).

# 4.3 State-estimation, Kalman filtering and the Linear-Quadratic-Gaussian Regulator (LQG)

In this section, we will finally implement an LQG controller with a Kalman filter to estimate the states we could not know and filter the noise out.

The system is:

$$\tilde{\dot{x}} = A\tilde{x} + B\tilde{u} + Mw,\tag{20}$$

$$y = C\tilde{x} + v, (21)$$

with V and W the covariance matrices of the v and w white noises such that:

$$E[w(t)w^{T}(t)] = W\delta(t), \ E[v(t)v^{T}(t)] = V\delta(t), \ E[w(t)v^{T}(t)] = 0.$$
 (22)

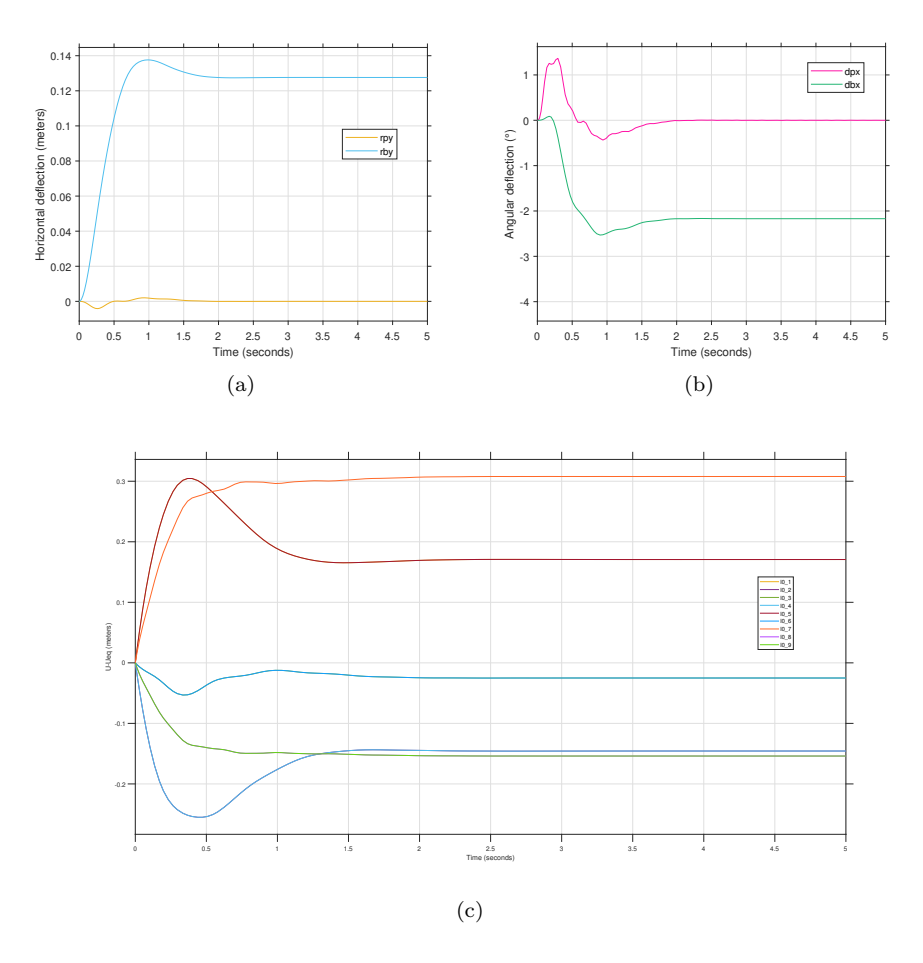


Figure 7: LQI control (a) Horizontal deflection (b) Angular deflection (c) Rest lengths changes with respect to their equilibrium values

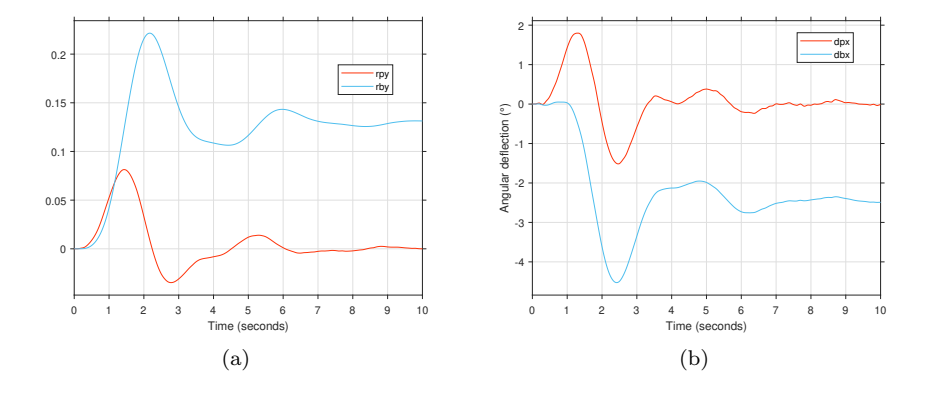


Figure 8: LQG (a) Horizontal deflection (b) Angular deflection

We look for a command u(t) that minimizes the following criterion:

$$\lim_{T \to \infty} E\left[\int_0^T x^T Q x + u^T R u \, dt\right],\tag{23}$$

with

$$Q = Q^T \ge 0, \ R = R^T > 0. \tag{24}$$

The system was able to estimate all the unknown states (the horizontal displacement and angular deflection of the payload being the only ones measured), and we see in figure 8 that the system could also filter the noise out. Because, as with LQI, we augmented the system with the integrated states that matter, we can also achieve perfect stabilization of the known states after a time that can be set by the tunable  $T_c$  parameter introduced in equation (18). All the goals for the controlled system are therefore achieved.

#### 5 Conclusion

In summary, the paper formulated the statics and dynamics of the planetary-explorer balloon-payload system. Model-based control laws with LQR, LQI and LQG were applied, finding that it is indeed possible to actuate the whole structure, estimate the unknown states, filter the noise out and achieve zero steady-state error on the payload states. This can be done independently of the wind magnitude and direction, only by measuring the three translational and three rotational states of the payload.

#### 6 Future work

As the system simulated here is only in its very early days, a lot of questions still remain open. For example, what happens if one of the tethers go slack during the actuation? It must then be applied an optimization algorithm, dealing with linear matrix inequalities, to have all the tensions above a certain threshold, but also to minimize the maximum tension and therefore avoid tether breaking.

However, solving a linear problem but with non-linear constraints will require a lot of time, especially in embedded robotics, and we would lose the real time actuation. To solve this issue, the next work on this project will be to implement and train offline a deep neural network that would learn from the slow optimization solver. So that the output response could be found extremely fast when online and we may be able to recover real time actuation. It could help reducing the noise as well.

Finally, as already done in [9], other networks could be added to predict the wind magnitude and direction, and would therefore help being more precise in the commands to send. For example, recurrent convolutional neural networks making use of vision from a camera looking at a flapping flags attached to the different subsystems could be one idea.

#### 7 Acknowledgments

The authors gratefully acknowledge funding from Jet Propulsion Laboratory, California Institute of Technology, under a contract with the National Aeronautics and Space Administration (NASA) in support of this work.

#### References

- Greaves, J.S., Richards, A.M.S., Bains, W. et al. Phosphine gas in the cloud decks of Venus. Nat Astron (2020). https://doi.org/10.1038/s41550-020-1174-4.
- [2] B. Kennedy, Y.Cheng, H. Aghazarian, M. Garrett, "LEMUR: Legged excursion mechanical utility rover", *Autonomous Robots*, November 2001.
- [3] P. Abad-Manterola, J. A. Edlund, J. W. Burdick, A. Wu, T. Olivier, I. A.D. Nesnas, J. Cecava, "A Minimalist Tethered Rover for Exploration of Extreme Planetary Terrains", *IEEE Robotics Automation Magazine*, December 2009, Vol 44.
- [4] Valles Marineris, Jezero Crater, Araneiforms and gully deposits in Hale Crater, available at: https://mars.nasa.gov/resources/3874/valles-marineris/, https://www.nasa.gov/image-feature/jezero-crater-mars-2020s-landing-site, https://www.nasa.gov/image-feature/jpl/jamming-with-the-spiders-from-mars and https://www.nasa.gov/image-feature/jpl/bedrock-exposed-in-the-rim-of-hale-crater.
- [5] R. Motro, "Tensegrity: from Art to Structural Engineering", IASS-APCS Symposium, May 2012, Séoul, South Korea.
- [6] R. Skelton, M. De Oliveira. Tensegrity Systems., 2009.
- [7] T. Bewley, UC San Diego, NASA Jet Propulsion Laboratory (2019). Stabilization of low-altitude balloon systems, Part 2: riggings with multiple taut ground tethers, analyzed as tensegrity systems., 2019.
- [8] P. de Larminat. Automatique. Commande des systèmes linéaires. Traité des nouvelles technologies Série automatique. Hermès, première édition, 1996.
- [9] J. Cardona, M. Howland, J. Dabiri. Seeing the Wind: Visual Wind Speed Prediction with a Coupled Convolutional and Recurrent Neural Network., 2019.
- [10] D. Alazard, C. Cumer, P. Apkarian, M. Gauvrit, G. Ferreres. *Robustesse et Commande Optimale*, Supaéro, Cépaduès Editions, 1999.
- [11] P. Chevrel, M. Yagoubi, F. Claveau *IMT Atlantique courses*, IMT Atlantique, 2019.
- [12] M. De Oliveira. Graduate Teaching courses, UCSD, 2019.
- [13] T. Bewley. Numerical Renaissance, Renaissance Press, 2018.
- [14] A. Zhang, Z. Lipton, M. Li, A. Smola. Dive into Deep Learning, 2019.

[15] A. Robey, H. Hassani, G. Pappas. *Model-Based Robust Deep Learning*, 2020.